Title: A new perspective on slow pacemaking in brain and heart

Authors: Arthur Fyon[1], Oleksandra Pavlova[2], Nick Schaar[3], Pietro Mesirca[4], Amandine Ligot[2,4], Marvin Gaillardon[4], Julien Brandoit[1], Sofian Ringlet[5], Alessio Franci[1,6], Matteo E. Mangoni[4], Jochen Roeper[3], Guillaume Drion[1†], Vincent Seutin[2*†] & Kevin Jehasse[1*†]

Affiliations:

[1]Neuroengineering laboratory, Montefiore Institute, University of Liège, Belgium.

[2]Laboratory of Neurophysiology, GIGA Institute, University of Liège, Belgium.

[3]Institute of Neurophysiology, Neuroscience Center, Goethe University, Frankfurt am Main, Germany.

[4]Institut de Génomique Fonctionnelle, Université de Montpellier, CNRS, INSERM, France.

[5]Laboratory of Molecular Regulation of Neurogenesis, GIGA Institute, University of Liège, Belgium.

[6]WEL-T Department, WEL Research Institute, Belgium.

[†]denotes equal contribution

Abstract

Slow pacemaking is a key physiological process in specific excitable cells, yet its underlying mechanism remains debated. Here we identify a conserved, voltage-dependent pacemaker current that is essential for slow, regular firing in both midbrain dopaminergic neurons and sinoatrial node myocytes. Conductance-based models incorporating this current reproduce stable pacemaking, requiring a fast-activating, small-amplitude current. This is further confirmed by dynamic-clamp experiments in dopaminergic neurons. Replacing the pacemaker current in a model with a voltage-independent conductance such as the non-selective sodium leak channels fails to sustain slow rhythmicity, highlighting the necessity for an adequate voltage dependence. Our results suggest a novel and shared biophysical mechanism for slow pacemaking in neuronal and cardiac systems.

Main Text:

Introduction

Pacemaking is a fundamental property of a subset of excitable cells that underpins vital rhythmic functions across biological systems. Pacemaker cells can be classified, based on the firing frequency, as either fast or slow pacemakers. While the mechanism sustaining fast pacemaking is known [1], slow pacemaking remains controversial. It has been suggested that it originates from the balanced interplay between several depolarizing and hyperpolarizing currents [2–6]. The main ionic currents involved in pacemaking are hyperpolarization-activated cyclic nucleotide-gated (HCN encoding I_H in neurons and I_F in cardiac cells) and voltage-gated Ca^{2+} (Ca_v) and Na^+ (Na_v) channels underlying inward currents on the one hand, and A-type (I_A) fast inactivating, ERG-type (I_{Kr}), or KvLQT (I_{Ks}) K^+ channels, underlying outward currents on the other hand. Yet, experimental data shows that blocking or altering any of ion channels driving inward current, do not abrogate slow pacemaking, although both its frequency and regularity can be affected [3,7–12]. Another hypothesis is that the production of such a precise (coefficient of variation below 5%) and robust low frequency (1-5 Hz on average) pacemaking needs the reliable activation of a pacemaker current (I_{pace}) during the interspike interval [1,7,13–16]. Yet the nature, dynamics, and origins of such an essential current have remained elusive. Recently, we found that a compound previously shown to block gating pore currents, 1-(2,4-xylyl)guanidinium (XG), abrogates pacemaking of rodent midbrain dopamine neurons (mDANs) [7]. Using voltage ramps and pacemaker-clamp, we were able to isolate the tiny current blocked by XG, reminiscent of the elusive I_{pace}. Since slow pacemaking is such a fundamental behavior for life, we hypothesized that this mechanism is conserved across neuronal and cardiac pacemaker myocytes and species. We therefore investigated whether similar effects of XG would be observed in human mDANs and in rodent sinoatrial node (SAN) pacemaker myocytes and found it to be the case. Dynamic-clamp experiments, in which electrophysiological recordings are coupled to exogenous current injections to either add or subtract conductances, confirmed that the XG-sensitive I_{pace} is necessary and sufficient for slow pacemaking. Next, we used both a conductance-based model of a mDAN [17] and a reduced neuronal model and showed that the voltage dependence of I_{pace} is ideally suited to be the effector of slow pacemaking. Taken together,

our data supports the hypothesis of a conserved mechanism for slow pacemaking, encompassing neuronal and cardiac pacemaker cells.

Results

Evidence for a shared mechanism of slow pacemaking across species and systems

We had previously shown that pacemaking of rodent mDANs is blocked by XG and had isolated the current sensitive to XG (**Fig. 1A-C**) [7]. We first asked whether pacemaking in human mDANs derived from two different induced pluripotent stem cells (hIPSCs) lines (see *Methods*) would be similarly affected by the drug. These neurons were identified as mDANs based on their spontaneous slow firing frequency, hyperpolarization by dopamine and, in some cases, the expression of tyrosine hydroxylase (**Fig. S1**; see *Methods*). Upon superfusion of XG, their spontaneous activity was silenced (2.28 ± 0.44 Hz in control vs 0.12 ± 0.05 in XG, n = 9, p = 0.0039, Wilcoxon test; **Fig. 1D, E**), similarly to what we had observed in rodent models. In particular, as in rodent mDANs, the silencing of the electrical activity by XG does not involve membrane hyperpolarization, contrary to what is seen with dopamine, which is known to open G-protein-coupled inwardly rectifying channels in these cells (**Fig. S1**). Moreover, we observed a current sensitive to XG in human mDANs which is similar to the one observed in rat mDANs (**Fig. 1F**). Taken together, these results suggest that the mechanism of pacemaking is conserved across species in this cell type.

To investigate whether this finding could be extended to another cell type endowed with pacemaking, we explored the case of SAN pacemaker myocytes of the heart, which are also slow (1-5 Hz), very regular, pacemakers. In addition, similar to mDANs, these cells express high levels of L-type $Ca_v1.3$ and HCN channels [5]. Upon superfusion of XG, we observed a marked decrease of pacemaking in SAN myocytes (from 166.5 ± 9.1 bpm in control to 24.5 ± 10.1 bpm in XG, n = 11, p = 0.001, Wilcoxon test; **Fig. 1G, H**). Slowing of pacemaker activity by XG could not be attributed to interaction with delayed-rectifier K^+ currents, the L- and T-type Ca^{2+} current (I_{CaL} and I_{CaT}), nor with HCN-mediated I_f current (**Fig. S2**), but to inhibition of a tiny inward "pacemaker" current that we refer to as $I_{pace.}$ In SAN myocytes, I_{pace} showed similar characteristics to those previously observed in mDANs (**Fig. 1I, J**), including activation at negative voltages (-50 mV), voltage-dependent current increase along the diastolic depolarization voltage range (corresponding to the neuronal interspike) and peaking at ~-20 mV, a voltage more depolarized than the

threshold of the action potential in both cell types. Moreover, XG inhibited the spontaneous activity of isolated SAN pacemaker myocytes with apparent concentration for half-inhibition (IC_{50}) of 32 μM, smaller than what we previously observed in rodent mDANs from acute brain slices [7]. The Hill coefficient was 2.5 (**Fig. S2D**). Consistently, XG decreased the spontaneous pacemaking rate of isolated Langendorff-perfused hearts (**Fig. S2E**). Taken together, these data indicate XG-sensitive I_{pace} as a shared mechanism for slow pacemaking in mDANs and in SAN pacemaker myocytes.

Modeling the pacemaker current confirms its ability to sustain slow pacemaking

We used a well-established conductance-based model to study slow pacemaking (**Fig. S3A, B**) [17]. Since this model is set to pace steadily without a pacemaker current, it relies on shifting the activation curve of Na^+ (g_{Na}) and L-type Ca^{2+} (g_{CaL}) conductances to artificially hyperpolarized potentials. We adjusted these activation curves to their measured physiological values in mDANs [18,19] (**Fig. S3C**), which led to a loss of spontaneous firing and a shift from type I to type II excitability (**Fig. S3B**). We then modeled the pacemaker conductance (g_{pace}) from the current-to-voltage curve of the XG-sensitive I_{pace} (**Fig. S3D**) and implemented it into the adjusted model (**Fig. S3E**). We were able to recover pacemaking activity with a voltage range of activation of g_{pace} similar to what had been observed experimentally (**Fig. 2A, B**) [7], as well as to recover type I excitability **(Fig. S3B**). Currentscape analysis [20] revealed the crucial contribution of g_{pace} during pacemaking (**Fig. 2A**). We then measured the total current between two spikes and observed that the resulting current is driven by g_{pace} (**Fig. 2B**) and has a small amplitude similar to previous experimental observations in mDANs [21]. Finally, we measured the charge transfer of each conductance during an interspike interval and a full cycle (**Fig. 2C**). Interestingly, the charge carried by g_{pace} (-191 fC) is much smaller than the charge carried by other conductances such as g_{CaL} (-1458 fC) or H-type conductance (g_H) (-2077 fC) during the interspike interval. Overall, these data highlight the essential role of the small conductance g_{pace} in slow pacemaking.

We next investigated the dynamical range of g_{pace} which is necessary to maintain a steady low frequency spontaneous activity (**Fig. 2D**). We explored both the density and activation time constant of g_{pace}, relative to the activation of Na_v channels, and found that the model remains stable as long as the activation of g_{pace} is very fast, close to instantaneous. Moreover, g_{pace} can have a wide range of densities, making the phenomenon robust. To

verify that these observations are not limited to the particular parameters used, we performed the same analysis using random parameters in which slow pacemaking can be observed (**Fig. S4**). In all cases, we observed similar requirements for the parameters of g_{pace}. Moreover, the addition of g_{pace} into the model increased ion channel degeneracy (**Fig. S5**), especially for g_{Na} and g_{CaL}, suggesting that it may stabilize neuronal output in the face of biological variability [22–25].

To further explore the structure of this increased degeneracy, we performed principal component analysis on the pacemaking solutions of the adjusted model. The analysis revealed no preferred direction of variability, indicating that the contribution of g_{pace} does not impose a dominant constraint on the system but instead distributes flexibility across all conductances (**Fig. S5C**). This isotropic degeneracy suggests that slow pacemaking remains robust even when the underlying ion channel expression varies extensively, emphasizing the stabilizing role of g_{pace} in maintaining reliable activity.

Dynamic clamp experiments confirm that g_{pace} is necessary and sufficient for slow pacemaking

Next, we used the dynamic-clamp approach to test how g_{pace} regulates slow pacemaking in spontaneously active mDANs from *substantia nigra pars compacta* (*SNc*) recorded *ex vivo* (**Fig. 3A**). First, we injected several values of negative conductance and evaluated the percentage of decrease in firing frequency (**Fig. 3B**). We observed a frequency decrease of 50% at -0.06 nS and complete silencing at -0.3 nS (1.54 Hz in control vs. 0 Hz with g_{pace} = - 0.3 nS, n = 20, N = 3, p = <0.0001, Wilcoxon test ; **Fig 3B**). Injecting positive values for g_{pace} increased the firing frequency as expected, leading to a depolarization block at the highest value tested (above 0.3 nS, **Fig. 3C**). Finally, we preincubated *SNc* DANs with XG to silence their activity and injected positive g_{pace} to test whether we could rescue slow pacemaking (**Fig. 3D**). Overall, the rescue was successful in all trials (n = 11) at a variable intensity of g_{pace} which is to be expected because of the diversity of the biophysical properties of mDANs [26]. Finally, we investigated the kinetics of g_{pace}. mDAN pacemaking was first silenced with XG and we rescued the activity upon g_{pace} injection (**Fig.4A, upper panel**). However, when changing the activation time from 1 ms to 30 ms at a constant conductance value, we observed that mDANs are more likely to generate a depolarization block with slower dynamics (**Fig. 4A-C**). This is entirely consistent with our model (**Fig. 4D**). The latter experiment demonstrates that our

modeling and experimental data are congruent and confirm that a fast and tiny current is required for slow pacemaking.

Respective roles of I_{pace} and other conductances for slow, regular pacemaking

We next sought to understand how important g_{pace} is for slow pacemaking. We reduced our conductance-based model to a minimal one, keeping only g_{Na} and g_{Kd} for spike generation, as well as g_{LNS} (leak conductance) to set the membrane at the desired potential. Adding g_{pace} in this minimal configuration enabled slow pacemaking similarly to our complete model (**Fig. 5A**). In this model, slow pacemaking is still maintained with fast activating g_{pace} over a wide range of densities, from 4.5 mS/mm² to 35.5 mS/mm² (**Fig. 5B**). Since our data showed that this minimal configuration is sufficient to create slow pacemaking, we investigated the role of the other conductances, especially A-type K^+ (g_{KA}), H-type (g_H) and Ca^{2+}-dependent K^+ (g_{KSK}) conductances. These have been shown in slices to help maintaining the firing frequency and regularity constant during membrane potential changes caused by excitatory and inhibitory inputs [3,21,27]. We introduced current noise in our minimal model and observed that the pacemaking becomes irregular (**Fig. 5C**). In our complete model, the firing frequency is robust to current injection, similarly to what has been observed by others [3,21,27]. Moreover, we also observed that these conductances, and especially g_{KSK}, help to reduce the slope of the firing frequency – injected current relationship, which is expected (**Fig. 5D**).

We then challenged the requirement of a voltage-gated activation for g_{pace} in order to obtain slow pacemaking. We replaced g_{pace} by a linear leak conductance similar to NALCN channels (g_{Nalcn}), as they had been suggested by some authors to be the main drivers of pacemaking in some mDANs [13,28–30]. g_{Nalcn} failed to sustain slow pacemaking (**Fig. S6**). In fact, low or high density of g_{Nalcn} could not generate spontaneous firing (**Fig. S6B**), while activity could be observed in a small window of density, going from type II excitability to fast pacemaking type I excitability (**Fig. S6C**). Our data therefore supports the notion that slow pacemaking requires a current with a specific voltage-dependent activation during the interspike interval, not a linear one.

Discussion

Slow pacemaking is a unique property which is observed in a subset of cells that play a major role in rhythmic biological processes. However, the precise mechanism(s) underlying slow pacemaking is (are) still controversial. Recently, we found that XG inhibits

189 the pacemaking of rodent mDANs and were able to isolate the current blocked by this
190 compound [7]. Here we show that this effect can be extended to human mDANs and to
191 mouse SAN pacemaker myocytes. Remarkably, the XG-sensitive conductance or g_{pace}
192 has very similar voltage-dependence in mDANS and SAN myocytes, starting to operate
193 at ~-50 mV and slowly increasing in amplitude towards more depolarized potentials. In
194 our minimal conductance-based model, we show that such a voltage dependence is able
195 to generate slow pacemaking, whereas addition of a linear conductance such as NALCN
196 is unable to induce this firing pattern.
197 In our adjusted conductance-based model of a mDAN, we show that addition of g_{pace} is
198 able to induce biologically realistic pacemaking. The properties of g_{pace} allow to extend
199 ion channel degeneracy, which makes our model more robust to biological variability (**Fig.**
200 **S5**). In this work, we describe key properties that I_{pace} should have. First, its activation
201 should be fast. Second, its amplitude can vary within a relatively large range, which
202 guarantees robustness. In addition, we show that, while large membrane conductances,
203 such as g_{CaL}, g_{KA} or g_H are not required for slow pacemaking [3,7], I_{pace} is sufficient to
204 generate slow automaticity in both the minimal and complete models.
205 Dynamic-clamp experiments confirmed the importance of g_{pace} (**Fig. 3**). Moreover, the
206 range of conductances to either rescue slow pacemaking upon XG perfusion or to silence
207 neuronal activity was a small fraction of the cell conductance, around 3 nS in rodent
208 mDANs [7]. Overall, setting g_{pace} to 0.3 nS was enough in both the negative conductance
209 and rescue experiments, confirming the fact that pacemaking relies on a tiny current.
210 These data support our hypothesis that the pacemaker channel should have a unitary
211 conductance value in the fS range [7,14]. In fact, if g_{pace} were to have a single channel
212 conductance similar to the main pore of Na_v channels (around 20 pS), it would imply that
213 slow pacemaking is sustained by at most 15 channels. Because of intrinsic stochasticity
214 of voltage-dependent channel gating, this would lead to very irregular firing in neurons
215 and in the heart.
216 In mDANs, the role of several ion channels in pacemaking has been investigated over the
217 years. L-type Ca_v channels were considered, since their pharmacological blockade with
218 high concentrations of dihydropyridines silenced these neurons [31–33]. Further studies
219 employing lower, pharmacologically relevant concentrations of L-type blockers did not
220 confirm these previous data [7,8,34,35], therefore suggesting an off-target effect of

221 dihydropyridines at high concentrations. This is consistent with our numerical simulations
222 in the present study, since our minimal model predicts pacemaking without a Ca_v
223 conductance. L-type $Ca_v1.3$ channels are now considered as linear amplifier of the firing
224 frequency in mDANs [8]. NALCN channels were also considered as a pacemaker
225 mechanism, as they are expressed in most rhythmic neurons [36]. However, further studies
226 showed controversial results, in which NALCN gene deletion or pharmacological
227 blockade suppressed [28–30,37] or did not impact pacemaking activity [7,29]. In this regard, our
228 simulations show that a linear depolarizing conductance is unlikely to sustain stable
229 pacemaking.
230 SAN pacemaking has been linked to either voltage-dependent activation of HCN
231 channels, or to a process of spontaneous cyclical Ca^{2+} release by cardiac ryanodine
232 receptors coupled to the Na^+/ Ca^{2+} exchanger (a process referred to as the "Ca^{2+} clock"
233 [38]). However, genetic silencing of cardiac HCN channels leads to bradycardia and
234 arrhythmia [39], without arresting heart pacemaking. In addition to HCN channels and the
235 Ca^{2+} clock, L-type $Ca_v1.3$ channels [40] and T-type Cav3.1 [41] channels have been proposed
236 to provide inward current in the diastolic phase (corresponding to neuronal interspike
237 interval) to generate pacemaking. In this regard, further work indicated also that $Ca_v1.3$
238 channels (i) constitute the main route for entry of Ca^{2+} in diastolic phase, (ii) activate the
239 Ca^{2+} clock [42] and (iii) mediate up-regulation of pacemaking by catecholamines with HCN
240 channels [12]. However, concomitant genetic ablation of $Ca_v1.3$ and $Ca_v3.1$ channels
241 strongly reduces (~60%), but still does not abrogate SAN pacemaking, even under
242 conditions of HCN and Nav channel inhibition [11]. These data strongly suggest the
243 existence of an additional ionic mechanism supporting slow cardiac pacemaking and
244 accounting for persistence of automaticity when other ion channels involved in the
245 generation of diastolic depolarization are inhibited. The properties of I_{pace} in DA neurons,
246 including voltage dependency, insensitivity to gadolinium [7] and to inhibition of the
247 Na^+/Ca^{2+} exchanger, suggest that in the SAN, g_{pace} is not generated by TRPM4 [43] or
248 TRPC [44] channels, but rather accounts for a previously overlooked ionic mechanism of
249 pacemaking.
250 In conclusion, our study unravels a new ionic current underlying spontaneous electrical
251 activity, shines new light on the controversial mechanism of slow pacemaking in

252 excitable cells and indicates a commonality across systems, an observation that is very
253 novel and surprising.
254

255 ## References

256 1. Bean, B. P. Mechanisms of pacemaking in mammalian neurons. *J. Physiol.* **n/a**, (2024).
257 2. Marder, E. & Goaillard, J.-M. Variability, compensation and homeostasis in neuron and network function. *Nat.*
258 *Rev. Neurosci.* **7**, 563–574 (2006).
259 3. Amendola, J., Woodhouse, A., Martin-Eauclaire, M. F. & Goaillard, J. M. Ca 2+/cAMP-sensitive covariation of
260 I A and I H voltage dependences tunes rebound firing in dopaminergic neurons. *J. Neurosci.* **32**, 2166–2181
261 (2012).
262 4. Amarillo, Y., Zagha, E., Mato, G., Rudy, B. & Nadal, M. S. The interplay of seven subthreshold conductances
263 controls the resting membrane potential and the oscillatory behavior of thalamocortical neurons. *J.*
264 *Neurophysiol.* **112**, 393–410 (2014).
265 5. Mangoni, M. E. & Nargeot, J. Genesis and Regulation of the Heart Automaticity. *Physiol. Rev.* **88**, 919–982
266 (2008).
267 6. Lakatta, E. G., Maltsev, V. A. & Vinogradova, T. M. A Coupled SYSTEM of Intracellular Ca2+ Clocks and
268 Surface Membrane Voltage Clocks Controls the Timekeeping Mechanism of the Heart's Pacemaker. *Circ. Res.*
269 **106**, 659–673 (2010).
270 7. Jehasse, K. *et al.* The gating pore blocker 1-(2,4-xylyl)guanidinium selectively inhibits pacemaking of midbrain
271 dopaminergic neurons. *Neuropharmacology* **197**, 108722 (2021).
272 8. Shin, J. *et al.* Cav1.3 calcium channels are full-range linear amplifiers of firing frequencies in lateral DA SN
273 neurons. *Sci. Adv.* **8**, eabm4560 (2022).
274 9. BoSmith, R. E., Briggs, I. & Sturgess, N. C. Inhibitory actions of ZENECA ZD7288 on whole-cell
275 hyperpolarization activated inward current (If) in guinea-pig dissociated sinoatrial node cells. *Br. J. Pharmacol.*
276 **110**, 343–349 (1993).
277 10. Verheijck, E. E., van Ginneken, A. C. G., Wilders, R. & Bouman, L. N. Contribution of L-type Ca2+current to
278 electrical activity in sinoatrial nodal myocytes of rabbits. *Am. J. Physiol.-Heart Circ. Physiol.* **276**, H1064–
279 H1077 (1999).

11. Baudot, M. *et al.* Concomitant genetic ablation of L-type Cav1.3 (α1D) and T-type Cav3.1 (α1G) Ca2+ channels disrupts heart automaticity. *Sci. Rep.* **10**, 18906 (2020).
12. Torre, E. *et al.* L-Type Cav1.3 and HCN Channels Mediate Heart Rate Acceleration by Catecholamines. *Circ. Res.* https://doi.org/10.1161/CIRCRESAHA.125.327497 (2025) doi:10.1161/CIRCRESAHA.125.327497.
13. Khaliq, Z. M. & Bean, B. P. Pacemaking in Dopaminergic Ventral Tegmental Area Neurons: Depolarizing Drive from Background and Voltage-Dependent Sodium Conductances. *J. Neurosci.* **30**, 7401–7413 (2010).
14. Seutin, V., Jehasse, K. & Drion, G. An alternative mechanism for slow pacemaking. *J. Physiol.* **n/a**, (2024).
15. Campbell, D. L., Rasmusson, R. L. & Strauss, H. C. Ionic Current Mechanisms Generating Vertebrate Primary Cardiac Pacemaker Activity at the Single Cell Level: An Integrative View. *Annu. Rev. Physiol.* **54**, 279–302 (1992).
16. DiFrancesco, D. Pacemaker Mechanisms in Cardiac Tissue. *Annu. Rev. Physiol.* **55**, 455–472 (1993).
17. Yu, N. & Canavier, C. C. A Mathematical Model of a Midbrain Dopamine Neuron Identifies Two Slow Variables Likely Responsible for Bursts Evoked by SK Channel Antagonists and Terminated by Depolarization Block. *J. Math. Neurosci. JMN* **5**, 5 (2015).
18. Seutin, V. & Engel, D. Differences in Na+ conductance density and Na+ channel functional properties between dopamine and GABA neurons of the rat substantia nigra. *J. Neurophysiol.* **103**, 3099–3114 (2010).
19. Durante, P., Cardenas, C. G., Whittaker, J. A., Kitai, S. T. & Scroggs, R. S. Low-Threshold L-type Calcium Channels in Rat Dopamine Neurons. *J. Neurophysiol.* **91**, 1450–1454 (2004).
20. Alonso, L. M. & Marder, E. Visualization of currents in neural models with similar behavior and different conductance densities. *eLife* **8**, e42722 (2019).
21. Khaliq, Z. M. & Bean, B. P. Dynamic, Nonlinear Feedback Regulation of Slow Pacemaking by A-Type Potassium Current in Ventral Tegmental Area Neurons. *J. Neurosci.* **28**, 10905–10917 (2008).
22. Goaillard, J.-M. & Marder, E. Ion Channel Degeneracy, Variability, and Covariation in Neuron and Circuit Resilience. *Annu. Rev. Neurosci.* **44**, 335–357 (2021).
23. Fyon, A., Franci, A., Sacré, P. & Drion, G. Dimensionality reduction of neuronal degeneracy reveals two interfering physiological mechanisms. *PNAS Nexus* **3**, pgae415 (2024).
24. Drion, G., O'Leary, T. & Marder, E. Ion channel degeneracy enables robust and tunable neuronal firing rates. *Proc. Natl. Acad. Sci. U. S. A.* **112**, E5361–E5370 (2015).

308 25. O'Leary, T., Williams, A. H., Franci, A. & Marder, E. Cell Types, Network Homeostasis, and Pathological
309 Compensation from a Biologically Plausible Ion Channel Expression Model. *Neuron* **82**, 809–821 (2014).
310 26. Roeper, J. Dissecting the diversity of midbrain dopamine neurons. *Trends Neurosci.* **36**, 336–342 (2013).
311 27. Higgs, M. H., Jones, J. A., Wilson, C. J. & Beckstead, M. J. SK and Kv4 Channels Limit Spike Timing
312 Perturbations in Pacemaking Dopamine Neurons. *eNeuro* **10**, (2023).
313 28. Philippart, F. & Khaliq, Z. M. Gi/o protein-coupled receptors in dopamine neurons inhibit the sodium leak
314 channel NALCN. *eLife* **7**, (2018).
315 29. Cobb-Lewis, D. E., Sansalone, L. & Khaliq, Z. M. Contributions of the Sodium Leak Channel NALCN to
316 Pacemaking of Medial Ventral Tegmental Area and Substantia Nigra Dopaminergic Neurons. *J. Neurosci.* **43**,
317 6841–6853 (2023).
318 30. Um, K. B. *et al.* TRPC3 and NALCN channels drive pacemaking in substantia nigra dopaminergic neurons.
319 *eLife* **10**, e70920 (2021).
320 31. Puopolo, M., Raviola, E. & Bean, B. P. Roles of Subthreshold Calcium Current and Sodium Current in
321 Spontaneous Firing of Mouse Midbrain Dopamine Neurons. *J. Neurosci.* **27**, 645–656 (2007).
322 32. Nedergaard, S., Flatman, J. A. & Engberg, I. Nifedipine- and omega-conotoxin-sensitive Ca2+ conductances in
323 guinea-pig substantia nigra pars compacta neurones. *J. Physiol.* **466**, 727–747 (1993).
324 33. Chan, C. S. *et al.* 'Rejuvenation' protects neurons in mouse models of Parkinson's disease. *Nature* **447**, 1081–
325 1086 (2007).
326 34. Drion, G., Massotte, L., Sepulchre, R. & Seutin, V. How Modeling Can Reconcile Apparently Discrepant
327 Experimental Results: The Case of Pacemaking in Dopaminergic Neurons. *PLOS Comput. Biol.* **7**, e1002050
328 (2011).
329 35. Guzman, J. N., Sánchez-Padilla, J., Chan, C. S. & Surmeier, D. J. Robust Pacemaking in Substantia Nigra
330 Dopaminergic Neurons. *J. Neurosci.* **29**, 11011–11019 (2009).
331 36. Lu, T. Z. & Feng, Z.-P. NALCN: A Regulator of Pacemaker Activity. *Mol. Neurobiol.* **45**, 415–423 (2012).
332 37. Wang, J. *et al.* The cation channel mechanisms of subthreshold inward depolarizing currents in the mice VTA
333 dopaminergic neurons and their roles in the chronic-stress-induced depression-like behavior. *eLife* **12**, RP88319
334 (2024).
335 38. Lakatta, E. G. & DiFrancesco, D. What keeps us ticking: a funny current, a calcium clock, or both? *J. Mol.*
336 *Cell. Cardiol.* **47**, 157–170 (2009).

39. Mesirca, P. *et al.* Cardiac arrhythmia induced by genetic silencing of 'funny' (f) channels is rescued by GIRK4 inactivation. *Nat. Commun.* **5**, 4664 (2014).

40. Mangoni, M. E. *et al.* Functional role of L-type Cav1.3 Ca2+ channels in cardiac pacemaker activity. *Proc. Natl. Acad. Sci.* **100**, 5543–5548 (2003).

41. Mangoni, M. E. *et al.* Bradycardia and Slowing of the Atrioventricular Conduction in Mice Lacking CaV3.1/α1G T-Type Calcium Channels. *Circ. Res.* **98**, 1422–1430 (2006).

42. Torrente, A. G. *et al.* L-type Cav1.3 channels regulate ryanodine receptor-dependent Ca2+ release during sino-atrial node pacemaker activity. *Cardiovasc. Res.* **109**, 451–461 (2016).

43. Hof, T., Simard, C., Rouet, R., Sallé, L. & Guinamard, R. Implication of the TRPM4 nonselective cation channel in mammalian sinus rhythm. *Heart Rhythm* **10**, 1683–1689 (2013).

44. Ju, Y.-K. *et al.* Store-Operated Ca2+ Influx and Expression of TRPC Genes in Mouse Sinoatrial Node. *Circ. Res.* **100**, 1605–1614 (2007).

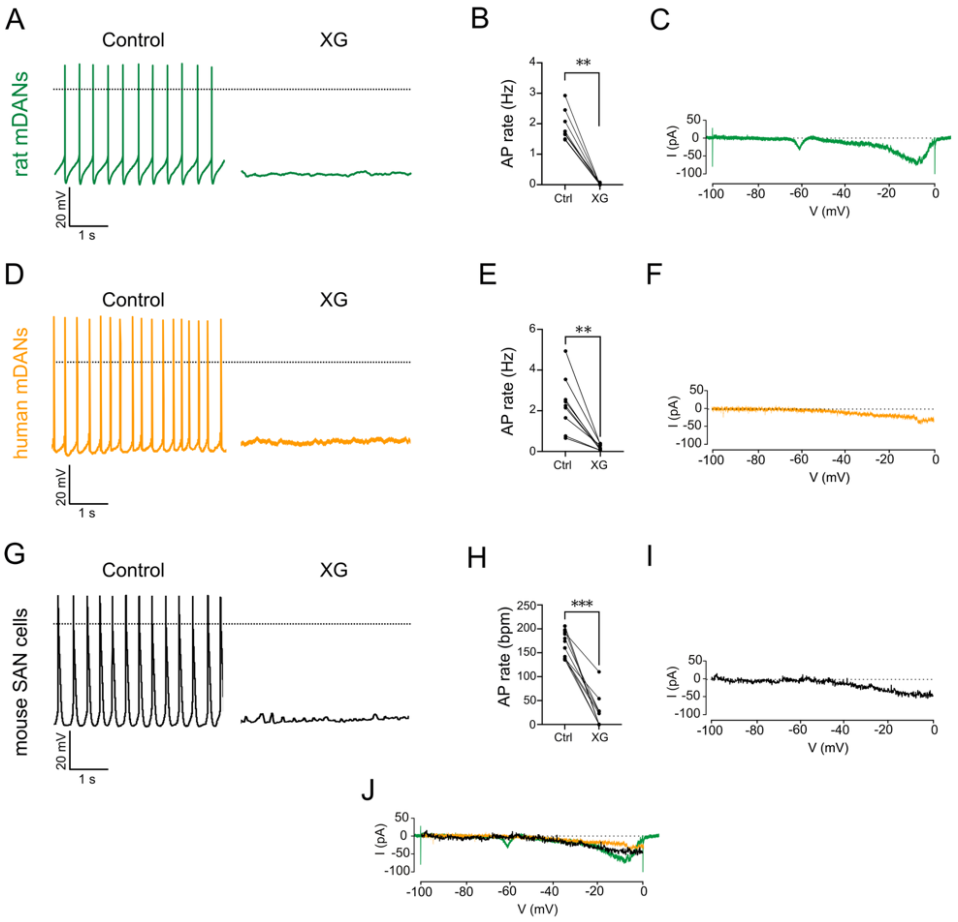

Fig. 1. XG inhibits slow pacemaker cells. (**A**) Pacemaking in rat mDANs is inhibited upon (2 mM) XG application. (**B**) Summary data of the effect of the application of 2 mM XG on the firing frequency. XG abolished the firing (1.94 ± 0.18 Hz in control vs 0.02 ± 0.001 Hz in XG, n = 8, p = 0.0078, Wilcoxon test). (**C**) XG-sensitive current isolated from rat mDANs. Inward current at -60 mV is the result from rundown of T-type calcium channels that was observed in one cell. (**A-C**) were adapted from *Jehasse et al. 2021* [7]. (**D**) Pacemaking in human mDANs is inhibited upon (600 µM) XG application. (**E**) Summary data of the effect of the application of 600 µM XG on the firing frequency (2.28 ± 0.44 Hz in control vs 0.12 ± 0.05 in XG, n = 9, p = 0.0039, Wilcoxon test). (**F**) XG-sensitive current isolated from human mDANs (**G**) Inhibition of pacemaking in mouse SAN myocytes by XG (300 µM) application. (**H**) Summary data of the effect of application of 600 µM XG on the spontaneous pacemaking of SAN myocytes, expressed in beats per minute (bpm). XG strongly reduces pacemaking (166.50 ± 9.11 bpm in control vs 24.55 ± 10.10 bpm in XG, n = 11, p = 0.001, Wilcoxon test). (**I**) XG-sensitive currents isolated from mouse SAN myocytes. (**J**) Overlay of XG-sensitive current from rat (green), human

368 mDANs (orange), and SAN myocytes (black) shows similarities in voltage activation and
369 current amplitude. Dashed lines correspond to 0 mV for voltage traces and 0 pA for
370 current traces.

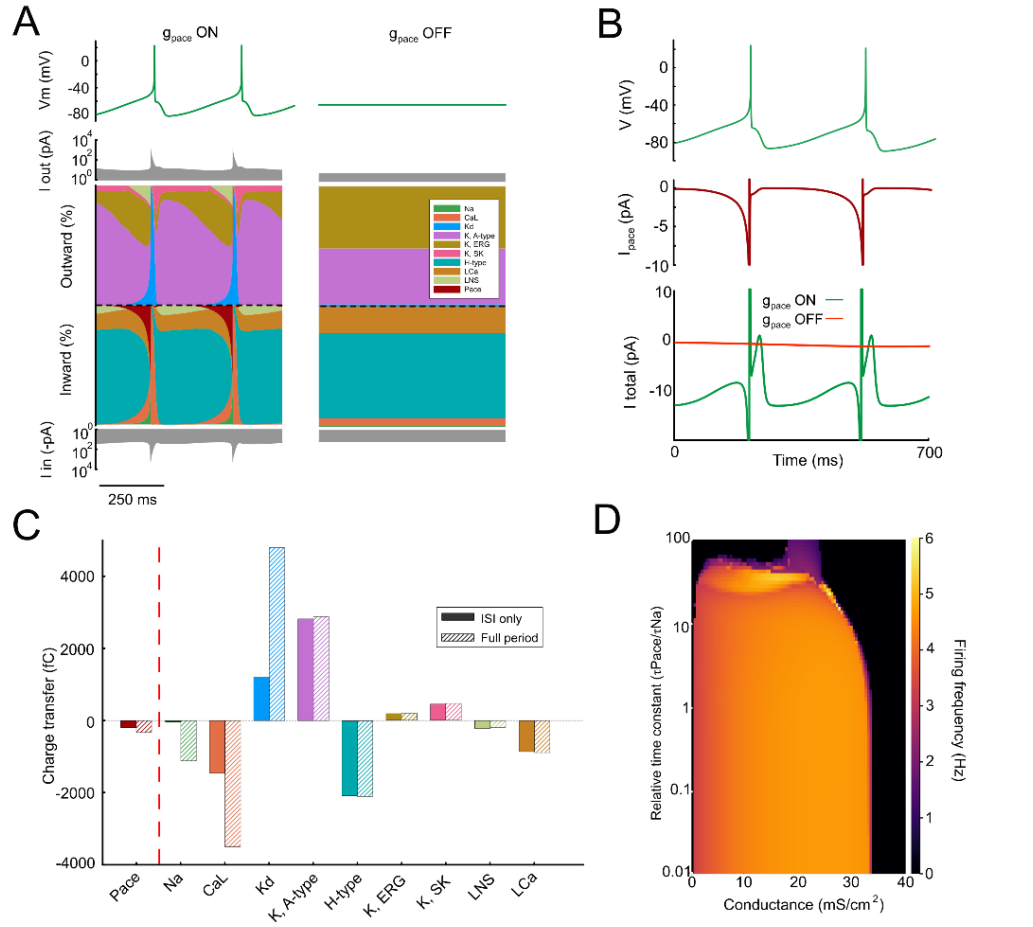

Fig. 2. Fast activating pacemaker conductance allows slow pacemaking in a mDAN conductance-based model. (**A**) Currentscape analysis reveals that, although its contribution seems small in comparison to other conductances, g_{pace} is crucial to generate slow pacemaking. (**B**) Simulated pacemaking activity in our adjusted pacemaking model (green) with I_{pace} dynamic below in red, showing a small amplitude during the interspike interval as previously observed [7]. Bottom panel corresponds to total current amplitude from our adjusted model with (green) and without (red) the addition of g_{pace}. The total current observed is similar to what has been calculated [13]. (**C**) Total charge transfer of each conductance during the interspike interval (ISI) and the full period of the simulation. Charge transfer was calculated by measuring the area under the curve in (**A**). (**D**) Heatmap analysis showing the multiplicative time constant of g_{pace} activation relative to g_{Na} according to the conductance density in which our adjusted model generates slow pacemaking.

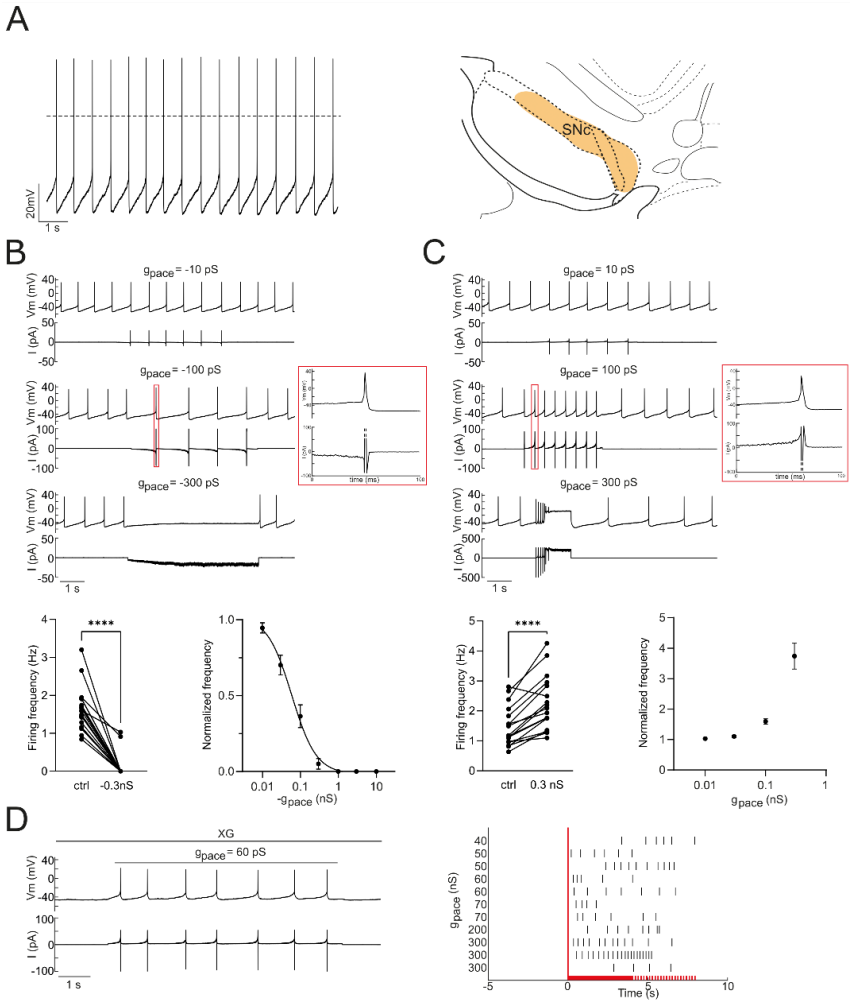

Fig. 3. The XG-sensitive conductance (g_{pace}) modulates pacemaking in *SNc* DANs. (**A**) *Ex vivo* pacemaking in a mouse *SNc* (orange shade) DAN. (**B**) Silencing of a *SNc* DAN upon injection of negative g_{pace} (upper panel). Summary data of the effect of negative g_{pace} on the firing frequency (lower panel). Negative g_{pace} abolished pacemaking at -0.3 nS (1,54 Hz (interquartile range: 1,193 - 1,864 Hz) in ctrl vs. 0 Hz (interquartile range: 0) with g_{pace} = - 0,3 nS, n = 20, N = 3, p = <0,0001, Wilcoxon test). (**C**) Excitation and overexcitation (depolarization block) of a *SNc* DAN upon positive g_{pace} (upper panel). Summary data of the effect of positive g_{pace} on the firing frequency (lower panel). g_{pace} increased the firing frequency (1,48 ± 0,66 Hz in ctrl vs. 2,26 ± 0,91 Hz with g_{pace} = 0,3 nS, n = 17, N = 3, p = <0,0001, paired t test). (**D**) Rescue of pacemaking after preincubation with (2 mM) XG and complete cessation of pacemaking. Firing pattern and g_{pace} value upon rescue display broad large variability (right). Time frame of steady state g_{pace} (bold red line). Time frame of manual deactivation of g_{pace} (discontinuous red line).

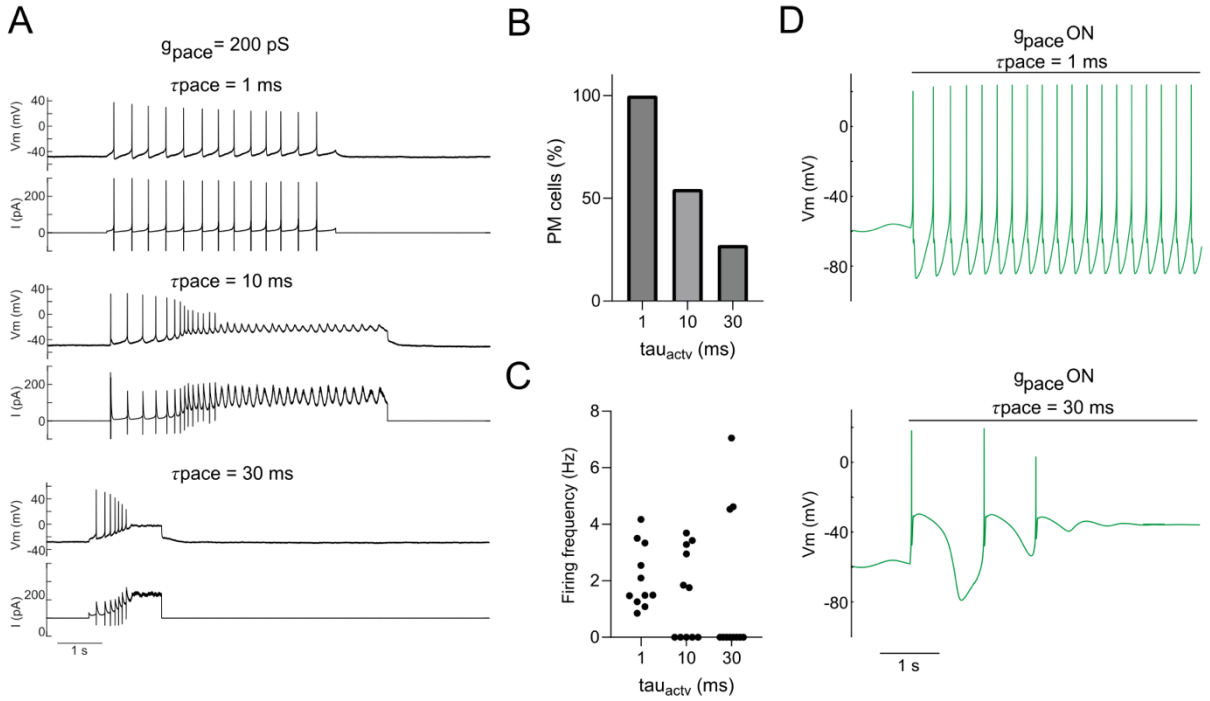

Fig. 4. The XG-sensitive conductance (g_{pace}) needs to be fast to obtain slow pacemaking. (**A**) Rescued pacemaking from mouse *SNc* DANs upon 2 mM XG superfusion. Increasing activation time of g_{pace} (τ_{pace}) generates a depolarization block. (**B**) Percentage of pacemaking cells decreases with slower activation time (n=11 for each group). (**C**) The amount of slow firing cells decreases with slower activation time (n=11 for each group). (**D**) Increased t_{pace} in our model generates a depolarization block, similarly to what we observed *in vitro*.

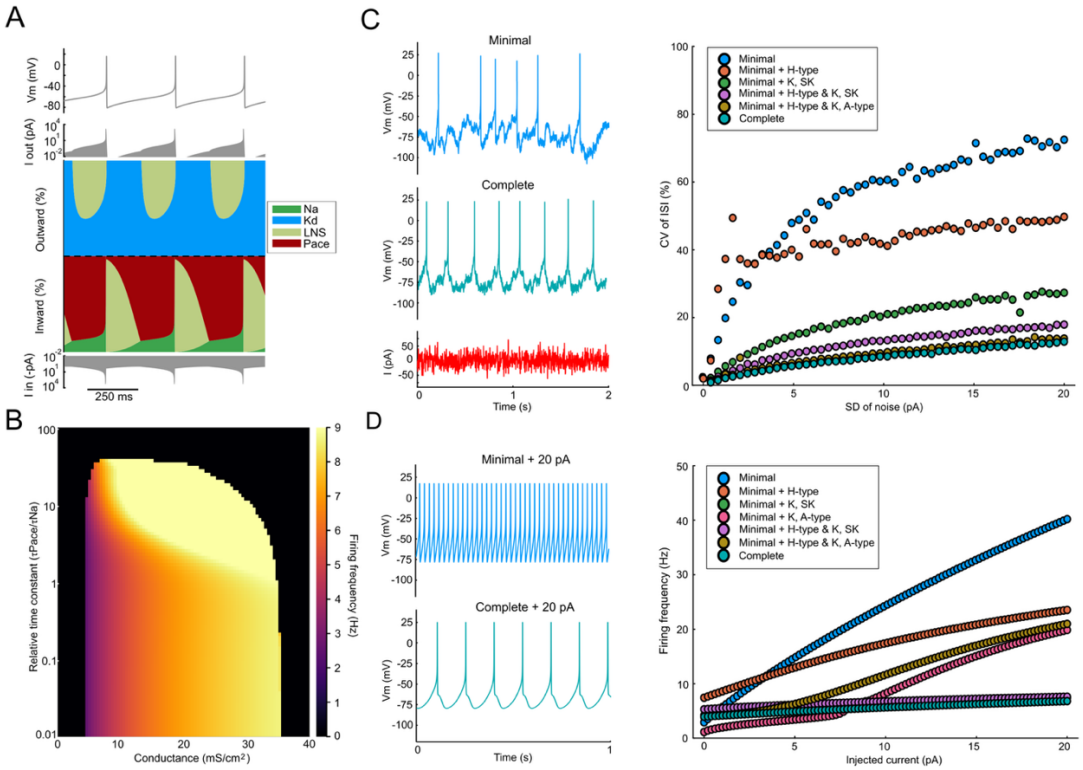

Fig. 5. Assessment of the conductances contribution in slow pacemaking. (**A**) Currentscape analysis from a minimal model including g_{Na}, g_{Kd}, g_{LNS} and g_{pace} shows that it is possible to generate slow pacemaking, similarly to what we observed *ex vivo* in the absence of other conductances [7], and that g_{pace} contribution is maximal during the interspike interval. (**B**) Heatmap analysis showing the multiplicative time constant of g_{pace} activation relative to g_{Na} according to the conductance density in which our minimal model generates slow pacemaking. (**C**) Robustness of slow pacemaking in response to noise (in red). In the minimal model (blue), current noise leads to irregular spiking, while the complete model (teal), current noise injection does not alter pacemaking regularity (left panel). Right panel corresponds to the effect of increasing the standard deviation (SD) of noise current to the coefficient of variation (CV) of the interspike interval (ISI). The addition of g_H, g_{KSK} and g_{KA} increases the robustness of slow pacemaking. In order to activate g_{KSK}, g_{LCa} was added. (**D**) Effect of the other conductances on the firing frequency upon continuous current injection. Left panel shows example of the firing frequency of the minimal (blue) and complete (teal) upon current injection of 20 pA. Right panel shows the effect of the combination of several conductances on the FI relationship. The results

related to g_{KSK} addition only are located behind the complete and combination of g_{KSK} and g_H data points.

Materials and Methods

Modeling

Programming language

The Julia programming language was used in this work [45]. Numerical integration was realized using *DifferentialEquations.jl*. Fitting was realized using *LsqFit.jl*. PCA was realized using *MultivariateStats.jl*.

Equation 1:

$$C\dot{V} = -\bar{g}_{Na}\, m^3\, h\, h_s\, (V - E_{Na}) - \bar{g}_{CaL}\, l\, (V - E_{Ca}) - \bar{g}_{Kd}\, n^3\, (V - E_K)$$
$$- \bar{g}_{KA}\, p\, \left(\frac{q_1}{2} + \frac{q_2}{2}\right) (V - E_K) - \bar{g}_{KERG}\, o\, (V - E_K) - \frac{\bar{g}_{KSK}}{1 + \left(\frac{0.00019}{[Ca^{+2}]}\right)^4} (V - E_K)$$
$$- \bar{g}_H\, m_H^2\, (V - E_H) - g_{LCa}\, (V - E_{Ca}) - g_{LNS}\, (V - E_{LNS}) + \frac{100\, I_{app}}{\pi\, d\, L}$$

Here, the dot notation represents time derivative (in /ms), V is the membrane potential (in mV), and C the membrane capacitance (in μF/cm²). The ionic currents are: I_{Na} (transient sodium), I_{CaL} (L-type calcium), I_{Kd} (delayed rectifier potassium), I_{KA} (A-type potassium), I_{KERG} (ether-à-go-go potassium), I_{KSK} (SK potassium), I_H (hyperpolarization-activated current), I_{LCa} (calcium leak), and I_{LNS} (non-specific leak). Reversal potentials are denoted by E. The intracellular calcium concentration $[Ca^{+2}]$ follows voltage-dependent kinetics as in (*13*). The soma geometry is defined by its diameter d and length L (in μm). The applied current is I_{app} (in pA).

Maximal conductances are denoted by the bar notation (in mS/cm²), representing the channel conductance when fully open. Gating variables follow first-order voltage-dependent kinetics of the following form.

Equation 2:

$$\tau_x(V)\, \dot{x} = x_\infty(V) - x$$

Here, x is the gating variable, $\tau_x(V)$ its voltage-dependent time constant, $x_\infty(V)$ its steady-state activation or inactivation function. Variables that were adjusted in this work are specified in the following section.

Unless otherwise stated, the original model parameters were used (Table S1) (*13*).

$$\bar{g}_{Na} = 6;\ \bar{g}_{CaL} = 0.139;\ \bar{g}_{Kd} = 1.117;\ \bar{g}_{KA} = 1.68;\ \bar{g}_{KERG} = 0.13;$$
$$\bar{g}_{KSK} = 0.07;\ \bar{g}_{H} = 0.078;\ \ g_{LCa} = 0.00245;\ g_{LNS} = 0.28;$$
$$C = 1;\ E_{Na} = 60; E_K = -90; E_{Ca} = 50; E_H = -29; E_{LNS} = -65; d = 15; L = 25$$

Adjustment of the mDAN conductance-based model and fitting of the pacemaking current

Before introducing the pacemaking current, activation of the transient sodium and L-type calcium channel was realized. In the original model (*13*), the steady-state activation functions were defined as follows.

Equation 3:

$$m_\infty(V) = \frac{1}{1 + e^{-\frac{V+30.09}{13.2}}};\ l_\infty(V) = \frac{1}{1 + e^{-\frac{V+45}{7.5}}}$$

These sigmoidal functions have half-activation voltages of −30.09 mV and −45 mV, respectively, which are substantially more hyperpolarized than values reported experimentally. In the adjusted model, both activation curves were shifted to −10 mV. The ultraslow inactivation of the transient sodium current (h_s) was disabled, as it was an adjustment to generate slow pacemaking in the original model [17].

The pacemaking current was fitted to a previously published voltage–current relationship (*3*) (**Fig. 1C**). The pacemaking current was modeled as a non-inactivating current, which provided an accurate fit without unrealistic parameter estimates.

Equation 4:

$$\begin{cases} I_{pace} = \bar{g}_{pace} m_{pace} \left(V - E_{pace}\right) \\ \tau_{m,pace}(V)\, \dot{m}_{pace} = m_{pace,\infty}(V) - m_{pace} \\ m_{pace,\infty}(V) = \dfrac{1}{1 + e^{-\frac{V - V_{half}}{V_{slope}}}} \end{cases}$$

Because the fit was performed on steady-state voltage–current data, no biological information was available on the time constant of pacemaking activation. We therefore set

Equation 5:

$$\tau_{m,pace}(V) = \alpha \cdot \tau_m(V)$$

where $\tau_m(V)$ is the activation time constant of the transient sodium current.

Fitting yielded the following parameter values, given to one decimal place.

$$\bar{g}_{pace} = 6.5;\ V_{half} = -13.3;\ V_{slope} = 6;\ E_{pace} = 4.3$$

Since this pacemaking conductance corresponds to a specific neuron, it was varied throughout the study to test robustness rather than fixed at the fitted value. Unless otherwise stated, the following parameters were used in the adjusted model.

$$\bar{g}_{Na} = 25;\ \bar{g}_{CaL} = 1;\ \bar{g}_{Kd} = 10;\ \bar{g}_{KA} = 1.68;\ \bar{g}_{KERG} = 0.13;\ \bar{g}_{KSK} = 0.3;$$

$$\bar{g}_{H} = 0.078;\ \ g_{LCa} = 0.00245;\ g_{LNS} = 0.28;\ \bar{g}_{pace} = 5;$$

$$C = 1;\ E_{Na} = 60; E_K = -90; E_{Ca} = 50; E_H = -29; E_{LNS} = -65; d = 15; L = 25$$

Modeling of a NALCN current

In **Fig. S6**, the NALCN conductance was modeled as a voltage-independent sodium current.

Equation 6:

$$I_{NALCN} = g_{NALCN}\,(V - E_{Na})$$

Degenerate population building

In **Fig. S5**, two degenerate populations (N=200) exhibiting pacemaking were generated for the original and adjusted models. The procedure was identical for both populations. All ionic conductances were randomly assigned using a uniform distribution between 0 and an upper bound value, corresponding to the ordinates of **Fig. S5B**. Each model was simulated and retained in the population if its firing frequency was between 1 and 5 Hz, if the spike peak exceeded 0 mV, and if the minimum membrane potential was between −90 and −60 mV.

<u>Cell Culture</u>

Cell lines

520 Two human induced pluripotent stem cell (hiPSC) lines were used in this study:
521 GM23338 (gift from Prof. Ira Mercedes Espuny Camacho, GIGA Neurosciences,
522 University of Liège) and a human TH-reporter iPSC line expressing mCherry (gift from
523 Dr. Aleksandar Rakovic, Institute of Neurogenetics, University of Lübeck) [46]. Prior to
524 differentiation, cells were maintained for 2–3 consecutive passages in E8 medium using
525 standard EDTA-based passaging when confluency reached 70–80%.
526
527 *Differentiation to midbrain dopaminergic neurons*
528 Differentiation was carried out using a slightly modified version of the protocol published
529 by Stathakos *et al*. (2019) [47]. Briefly, hiPSCs were cultured in E8 medium for up to 4
530 days before switching to neural induction medium consisting of N2B27 supplemented
531 with 100 nM LDN193189, 10 µM SB431542, 300 ng/mL SHH, and 0.6 µM CHIR99021.
532 This was considered neuralization day 0. Cells were passaged on polyornithine/laminin-
533 coated plates at days 3 and 7 using Accutase at a density of 4×10^4 cells/cm² in
534 induction medium with 10 µM Y27632 or 1:100 RevitaCell.
535 From day 11, the medium was replaced with progenitor expansion medium (N2B27 with
536 20 ng/mL BDNF, 20 ng/mL GDNF, 0.2 mM ascorbic acid, and 10 µM Y27632). Upon
537 confluence, cells were passaged every 3-4 days in this medium. Terminal differentiation
538 started on day 16 by seeding cells at 5,000 cells/cm² onto PO/laminin-coated coverslips
539 in N2B27 supplemented with 20 ng/mL BDNF, 20 ng/mL GDNF, 0.2 mM ascorbic acid,
540 500 µM db-cAMP, 10 µM DAPT, and 10 µM Y27632. Cells were allowed to attach for ~1
541 hour before flooding wells with the same medium. Media was refreshed every 3 days
542 with 50% volume exchange.
543
544 <u>Tissue preparation</u>
545 *Animals*
546 For dynamic-clamp experiments, adult male C57BL/6N (Charles River Laboratories)
547 mice (8 to 14 weeks of age) were used. A maximum of 5 mice were housed per cage
548 and single animal housing was avoided when possible. Animals were maintained on a
549 12-hour light-dark cycle and provided with water and food ad libitum. All experimental
550 procedures involving mice were approved by the German Regional Council of
551 Darmstadt.

552 For SAN cells experiments, the study is in accordance with the Guide for the Care and
553 Use of Laboratory Animals published by the US National Institute of Health (NIH
554 Publication No. 85-23, revised 1996) and European directives (2010/63/EU). All mice
555 used were from the C57BL/6J background (Charles River and Janvier labs).
556 Experimental procedures were approved by the Ethical Panel of the University of
557 Montpellier and the French Ministry of Agriculture (protocol no: 2017010310594939).
558 Animals were housed in the IGF animal facility with free access to food and water and
559 were exposed to 12 h light/dark cycles in a thermostatically controlled room (21–22 °C)
560 with 40−60% humidity.
561
562 *Slice preparation for mouse midbrain dopamine neurons*
563 Animals were anesthetized by intraperitoneal injection of ketamine (250 mg/kg; Ketaset,
564 Zoetis) and medetomidine hydrochloride (2.5 mg/kg; Domitor, OrionPharma) before
565 intracardial perfusion using ice-cold ACSF consisting of the following: 50 mM sucrose,
566 125 mM NaCl, 2.5 mM KCl, 25 mM $NaHCO_3$, 1.25 mM NaH_2PO_4, 2.5 mM glucose, 6
567 mM $MgCl_2$, 0.1 mM $CaCl_2$, and 2.96 mM kynurenic acid (Sigma-Aldrich), oxygenated
568 with 95% O_2 and 5% CO_2. Rostral coronal midbrain slices (bregma, −2.92 to −3.16 mm)
569 were sectioned into 250-µm slices using a vibrating blade microtome (VT1200s, Leica).
570 Before the experiment, slices were kept at 37°C for 1 hour in oxygenated extracellular
571 solution containing the following: 22.5 mM sucrose, 125 mM NaCl, 3.5 mM KCl, 25 mM
572 $NaHCO_3$, 1.25 mM NaH_2PO_4, 2.5 mM glucose, 1.2 mM $MgCl_2$, and 1.2 mM $CaCl_2$.
573
574 *Isolation of mouse sinoatrial node myocytes*
575 Sinoatrial node myocytes were isolated as previously described [48]. Briefly, Sinoatrial
576 tissue (SAN) strips were immersed into "low Ca^{2+}" Tyrode's solution containing (in mM):
577 140 NaCl, 5.4 KCl, 0.5 $MgCl_2$, 1.2 KH_2PO_4, 50 taurine, 5.5 D-glucose, 1 mg/mL BSA,
578 and 5 Hepes (adjusted to pH 6.9 with NaOH) for 5 min. The tissue was then transferred
579 into the low-Ca^{2+} solution containing Liberase TH (0.15 mg/mL, Roche) and Elastase
580 (0.48 mg/mL, Worthington). Digestion was carried out for 15-20 min at 36 °C. SAN
581 strips were then washed in "Kraftbrühe" (KB) solution containing 100 L-glutamic acid
582 potassium salt, 10 L-Aspartic acid potassium salt, 25 KCl, 80 KOH, 10 KH_2PO_4, 2
583 $MgSO_4$, 5 Creatine, 0.5 EGTA, 20 D-glucose, 20 taurine, 1 mg/mL BSA, and 5 Hepes

584 (adjusted to pH 7.2 with KOH). Single myocytes were isolated from the SAN tissue by
585 manual agitation using a flame-forged Pasteur's pipette in KB solution at 36 °C. For
586 recovering of pacemaker activity, Ca^{2+} was gradually reintroduced into the cells' storage
587 solution to a final concentration of 1.8 mM. Cells were then stored at room temperature
588 until use.
589
590 Electrophysiological Recordings
591 *Midbrain dopamine neurons*
592 For rat mDANs, the recordings were obtained from previous work [7]
593 For human mDANs, electrophysiological properties of differentiated neurons were
594 assessed using both on-cell and whole-cell patch-clamp recordings performed at 30°C
595 with a Multiclamp 700B amplifier and Clampex 11.1 software. The extracellular solution
596 contained (in mM): 140 NaCl, 5 KCl , 2 $CaCl_2$,2 $MgCl_2$,15 HEPES, and 10 D-glucose;
597 pH was adjusted to 7.3 with NaOH. The intracellular pipette (3-5 MΩ) solution contained
598 (in mM): 135 K-gluconate, 10 NaCl, 0.5 $CaCl_2$, 15 HEPES, 2 Na_2ATP, and 5 EGTA; pH
599 adjusted to 7.3 with KOH, osmolarity ~ 300 mosm. Putative *substantia nigra pars*
600 *compacta* (*SNc*)-type mDANs were identified by similar characteristic
601 electrophysiological features we used to identify rodent mDANs [7,49–51], including
602 spontaneous pacemaking activity (0.5–5 Hz), action potential duration > 1.35 ms
603 (measured at half-amplitude), a prominent hyperpolarization-activated inward current
604 (I_H), and membrane hyperpolarization > 5 mV in response to 100 μM dopamine from a
605 holding potential of -60 mV. I_H was observed in many, but not all neurons satisfying
606 these criteria. To test the inhibition of pacemaker activity, 600 μM of 1-(2,4-
607 xylyl)guanidinium mesylate (XG) was applied to the bath solution. XG was produced as
608 previously described [7].
609 For dynamic-clamp recordings in mouse *SNc* DANs, slices were placed in a heated
610 recording chamber (37°C) that was superfused with the oxygenated extracellular
611 solution with a flow rate of 2 to 4 ml/min. CNQX (20 μM), DL-AP5 (10 μM), gabazine (4
612 μM; SR95531), and were added to inhibit respectively excitatory and inhibitory synaptic
613 transmission. Neurons were visualized using infrared differential interference contrast
614 video microscopy with a digital camera (VX55, Till Photonics) connected to an upright
615 microscope (Axioskop 2, FSplus, Zeiss). Patch pipettes were pulled from borosilicate

616 glass (GC150TF-10, Harvard Apparatus, Holliston, MA, USA) using a temperature
617 controlled, horizontal pipette puller (DMZ-Universal Puller, Zeitz). Patch pipettes (3 to 5
618 MΩ) were filled with a solution containing the following: 135 mM K-gluconate, 5 mM
619 KCl, 10 mM HEPES, 0.1 mM EGTA, 5 mM $MgCl_2$, 0.075 mM $CaCl_2$, 5 mM Na
620 adenosine 5′-triphosphate, 1 mM Li guanosine 5′-triphosphate, and 0.1% Neurobiotin,
621 adjusted to a pH 7.35 with KOH. For pharmacology, slices were preincubated for at
622 least 10 min with XG mesylate (2 mM) before recording. Recordings were performed
623 using an EPC-10 patch-clamp amplifier (HEKA Elektronik) with a sampling rate of 20
624 kHz and a low-pass filter (Bessel, 5 kHz). For analysis, recordings were further digitally
625 filtered at 1 KHz. A real-time Linux-based data acquisition program (RTXI; http://rtxi.org)
626 was used to inject online calculated currents (acquisition rates of 10 kHz) of the
627 modelled XG-sensitive conductance according to the following equation:
628 *Equation 7*

629
$$\begin{cases} I_{pace} = \bar{g}_{pace} m_{pace} \left(V - E_{pace}\right) \\ \tau_{m,pace}\, \dot{m}_{pace} = m_{pace,\infty}(V) - m_{pace} \end{cases}$$

630

631 V is the membrane voltage in mV, E_{pace} the reversal potential in mV and g_{pace} is the
632 conductance in nS, according to the fit in **Fig.S3D**.
633

634 *Heart rate recordings in Langendorff-perfused mouse hearts*
635 We performed ECG recordings in isolated Langendorff-perfused mouse hearts as
636 previously described [52]. Mice were deeply anesthetized by intraperitoneal injection of
637 0.3 mL of physiological NaCl solution containing Ketamine (0.1 mg/g, Imalgène) and
638 Xylazine (0.01mg/g, Rompun 2%, Bayer), followed by a second injection of 0.3 mL of
639 solution containing Pentobarbital (150 µL Euthasol / 10 mL NaCl physiological solution).
640 0.5 mL of NaCl solution containing Heparin (25000 U.I) was injected to avoid the
641 formation of intracardiac blood clots. Hearts were removed via thoracotomy following
642 negativity of the tail sensitivity test. Hearts were cannulated with an aortic cannula,
643 mounted on a Langendorff apparatus. The heart was set in a recording chamber
644 (Warner Instruments, Harvard Apparatus, Holliston, Massachusetts, USA). During
645 recordings, the temperature was maintained at 36.5-37 °C by a two-way, bath and
646 perfusion pipette temperature controller (model TC-344B, Warner Instruments). The

647 ECG was continuously recorded with bipolar electrodes (model SNE 100, Science
648 Products, Hofheim, Germany) placed at the right atrium and apex, connected to a
649 recording amplifier (ADInstruments, Colorado Springs, Colorado, USA).
650
651 *Mouse sinoatrial node myocytes*
652 SAN cells were harvested in custom-made chambers with glass bottoms for cell
653 attachment and superfused with Tyrode solution containing (in mM): 140 NaCl, 5.4 KCl,
654 1 $MgCl_2$, 1.8 $CaCl_2$, 5.5 D-glucose and 5 Hepes (adjusted to pH 7.4 with NaOH).
655 warmed at 36°C before recording.
656 XG-sensitive, delayed-rectifier potassium ($I_{K,r}$) and "funny" (I_F) currents were recorded in
657 extracellular Tyrode's solution under the standard whole-cell configuration whereas
658 action potentials were measured by perforated patch clamp technique with escin (0.04
659 mg/mL, Sigma-Aldrich) also in extracellular Tyrode's solution. For I_F recordings, 2 mM
660 $BaCl_2$ was added to Tyrode's solution to block I_{K1}. Electrodes had a resistance of 3–4
661 MΩ when filled with a solution containing (in mM): 80 K-aspartate, 50 KCl, 1 $MgCl_2$, 2
662 $CaCl_2$, 5 EGTA, 5 HEPES, and 3 ATP-Na (adjusted to pH 7.2 with KOH). Seal
663 resistances were in the range of 2–5 GΩ.
664 Superfusion of pre-warmed (36°C) experimental solutions was achieved by using a
665 multi-MPRE8 heating pen (Cell Micro Controls) and data acquisition was performed
666 using Multiclamp 700B patch-clamp amplifiers connected to a Digidata 1322A interface
667 (Molecular Devices, Saint Jose, CA, USA).
668
669 Immunocytochemistry
670 The DA phenotype of neurons in the process of maturation was confirmed by
671 immunocytochemistry as described earlier [53] with the use of tyrosine hydroxylase (TH)
672 (Merck, AB152) and βIII tubulin (TUBB3)/ TUJ1 (BioLegend, MMS-435P) antibodies.
673 Samples were imaged using an inverted confocal microscope (Leica SP5), with a
674 resolution of 512 x 512 pixels, pixel size is 0.758 µm. A ratio of TH+/TUBB3+ was
675 measured by counting the number of TH+ or TUBB3+ cells, in order to assess the
676 maturation of the human mDAN culture [53].
677
678 Data analysis

679 Dynamic-clamp data was digitally filtered at 1 kHz and further exported as MAT-files
680 using Fitmaster (Heka Elektronik). Offline data analysis was performed using custom-
681 written scripts in MATLAB. Spike thresholds were determined using the first derivative of
682 the recording where dVm/dt ≥ 10 mV/ms. Spike thresholds, peaks and minima after
683 hyperpolarization potential were visually verified for each cell. The g_{pace}-modulated firing
684 frequency was averaged for the first three ISIs (frequency in Hz).
685 All statistical analysis were performed using GraphPad Prism 10.2.1. Non-parametric
686 Wilcoxon's tests and Friedman's test followed by Dunn's multiple comparison were
687 performed and data are reported as mean ± standard error of the mean (SEM) and as
688 median (interquartile range). Number of cells are denoted by n, number of animals used
689 as N.
690
691 **Data and materials availability:** All data are available in the main and supplementary
692 text. Codes for simulation can be found at https://github.com/arthur-
693 fyon/Pacemaking_DA_Fyon_2026
694
695 **Supplementary references**

696 45. Bezanson, J., Edelman, A., Karpinski, S. & Shah, V. B. Julia: A Fresh Approach to Numerical Computing.
697 *SIAM Rev.* **59**, 65–98 (2017).
698 46. Rakovic, A. *et al.* Electrophysiological Properties of Induced Pluripotent Stem Cell-Derived Midbrain
699 Dopaminergic Neurons Correlate With Expression of Tyrosine Hydroxylase. *Front. Cell. Neurosci.* **16**, (2022).
700 47. Stathakos, P. *et al.* Imaging Autophagy in hiPSC-Derived Midbrain Dopaminergic Neuronal Cultures for
701 Parkinson's Disease Research. in *Autophagy: Methods and Protocols* (eds Ktistakis, N. & Florey, O.) 257–280
702 (Springer, New York, NY, 2019). doi:10.1007/978-1-4939-8873-0_17.
703 48. Louradour, J. *et al.* L-Type Cav1.3 Calcium Channels Are Required for Beta-Adrenergic Triggered
704 Automaticity in Dormant Mouse Sinoatrial Pacemaker Cells. *Cells* **11**, 1114 (2022).
705 49. Philippart, F. *et al.* Differential Somatic Ca2+ Channel Profile in Midbrain Dopaminergic Neurons. *J. Neurosci.*
706 **36**, 7234–7245 (2016).
707 50. Destreel, G., Seutin, V. & Engel, D. Subsaturation of the N-methyl-D-aspartate receptor glycine site allows the
708 regulation of bursting activity in juvenile rat nigral dopamine neurons. *Eur. J. Neurosci.* **50**, 3454–3471 (2019).

51. Ringlet, S. *et al.* Glycine-gated extrasynaptic NMDARs activated during glutamate spillover drive burst firing in nigral dopamine neurons. *Prog. Neurobiol.* **249**, 102773 (2025).
52. Mesirca, P. *et al.* G protein-gated IKACh channels as therapeutic targets for treatment of sick sinus syndrome and heart block. *Proc. Natl. Acad. Sci.* **113**, E932–E941 (2016).
53. Borgs, L. *et al.* Dopaminergic neurons differentiating from LRRK2 G2019S induced pluripotent stem cells show early neuritic branching defects. *Sci. Rep.* **6**, 33377 (2016).

Acknowledgments

We thank our colleagues from the laboratories of Neuroengineering and Neurophysiology for their valuable input and help, especially L. Vandries for the histology of human mDANs. We are grateful to Pr. J-F Liégeois and Dr. R. Vitello for providing the mesylate salt of XG; Pr. C. Canavier & Dr. C. Knowlton for sharing the original code for the pacemaker model; B. Fischer, J. Sonntag, S. Betz, G. Amrhein and T. Wulf for technical assistance in this project; Dr. F.C. Wang, Dr. L. Nguyen & Pr. A. Monteil for their input on the manuscript.

Funding

This work was supported by the Belgian Government through the Federal Public Service (FPS) Policy and Support (BOSA) grant NEMODEI (NEuroMOrphic Design of Embodied Intelligence) (AFy, JB, AFr, GD, KJ); Fonds National de la Recherche Scientifique (FNRS, Belgium) grants ASP-REN40024838 (AFy), J.0148.19 and T.0188.22 (VS). AFy is a Postdoctoral Researcher of FNRS. Liège University “Strategic opportunity grant” R.DIVE 1142-J-P-A-02 (OP, VS); Fondation Léon Frédéricq (KJ); Deutsche Forschungsgemeinschaft (DFG) - CRC1451 (JR); *Fondation Leducq* TNE 19CV03 (MEM) and Agence Nationale de la Recherche (ANR-23-CE14-0009-01, to MEM).

Author contributions

Conceptualization: AFy, VS, GD & KJ;
Methodology: AFy, PM, MG, SR, JB, AFr, KJ;
Investigation: AFy, OP, NS, PM, AL, MG, & KJ;
Visualization: AFy & KJ;
Funding acquisition: VS, GD & KJ;

Project administration: VS, GD & KJ;
Supervision: JR, MM, VS, GD & KJ;
Writing – original draft: AFy & KJ;
Writing – review & editing: all authors

Competing interests

Authors declare that they have no competing interests.

Additional information

Supplementary Information is available for this paper

Corresponding authors

Correspondence and requests for materials should be addressed to VS (v.seutin@uliege.be) and KJ (kevin.jehasse@uliege.be).